Torsional Oscillations in Automotive Transmissions: Experimental Analysis and Modelling

Hindawi Publishing Corporation
Shock and Vibration
Volume 2016, Article ID 5721960, 14 pages
http://dx.doi.org/10.1155/2016/5721960

Research Article

Torsional Oscillations in Automotive Transmissions: Experimental Analysis and Modelling

Enrico Galvagno, Mauro Velardocchia, and Alessandro Vigliani

Dipartimento di Ingegneria Meccanica e Aerospaziale, Politecnico di Torino, Corso Duca degli Abruzzi 24, 10129 Torino, Italy

Correspondence should be addressed to Enrico Galvagno; enrico.galvagno@polito.it

Received 30 July 2015; Revised 21 December 2015; Accepted 28 December 2015

Academic Editor: Radoslaw Zimroz

The paper investigates the torsional oscillations of an automotive transmission system by means of an experimental test bench used to validate the proposed lumped parameter model. The rig consists of a Dual Clutch Transmission (DCT) and a Manual Transmission (MT) connected through the respective output shafts, while the excitation is provided by two electric motors, which are controlled in speed or torque. The experimental analysis includes the measurement of the external torques, applied by the two electric motors to the mechanical system, and the measurement of the system response in terms of angular speeds at different positions along the transmission line. The frequency response of the system is estimated from the experimental data and compared with the results of a 5-degree-of-freedom lumped parameter model, which proves to be adequate to describe the dynamic behaviour of the system up to a frequency of 200 Hz. The comparison between simulated results and experimental data shows good agreement, so the model can be used to predict the torsional vibrations of the transmission system in the linear field. Moreover, the effects of the nonlinearities associated with the mean value of the excitations are shown. Finally the influence of the selected gear ratio on the experimental frequency response is discussed.

1. Introduction

Automotive transmissions are commonly used to transfer mechanical power from the prime mover of the vehicle, most frequently an Internal Combustion Engine (ICE), to the wheels. Today's research is oriented towards more efficient and less polluting alternatives, yet ICEs still represent the most widely used onboard power source due to their relevant advantages, especially in terms of specific power, autonomy, and ease of refueling.

From a dynamic point of view, a drawback is the torque irregularity, mainly due to the combustion process itself and to the inertial loads of the reciprocating and rotating masses. These irregularities show a frequency spectrum quite rich in harmonic content, obviously related to the orders of the rotational speed. Hence, irregularities represent an excitation source for the torsional vibrations affecting the whole automotive driveline; these oscillations may result in diminished comfort or in undesirable noise (clonk, rattle, etc. [1]).

Usually carmakers face this problem through expensive on-board experimental tests aiming at finding out how to reduce undesired phenomena, often requiring a large number of runs. An alternative approach is offered by simulation: obviously the whole transmission has to be accurately modelled and the resultant torsional model needs experimental validation. Under these assumptions, torsional models of automotive transmission systems may prove to be essential tools to design and verify the vibrational behaviour of a powertrain. In fact, the knowledge of the transmission transfer function matrix allows predicting the torsional vibration level of the transmission components for a given engine type, in the whole working speed and torque range [2].

The problem of reducing noise and vibrations is widely investigated in all engineering fields: [3] presents a summary of a large study regarding the isolation improvement of many vibration isolation devices, using different structural configurations, based on compressing and torsion rubber elements.

In the automotive field, Dual Mass Flywheels (DMFs) represent examples of devices used to reduce vibrations: they are continuously improved through sophisticated innovations (e.g., inner dampers, slide shoes, or pendulum-type dampers [4]). The torsional dynamic behaviour of a DMF is investigated both numerically and experimentally in [5], where a lumped parameter model of the torsional test rig considering two different models for the DMF damping (viscous and hysteretic) is proposed.

Nonlinear torsional models are used to analyse automotive transmission rattle problems and find solutions to reduce noise, vibration, and dynamic loads. In [6], the authors show that the torsional stiffness and inertial distribution of such systems represent a numerically stiff problem. In addition, the clearance nonlinearities in the gear meshes result in discontinuous functions: both factors affect the efficacy of time domain integration and smoothening functions are widely used to overcome computational difficulties and improve the simulation. In [7], a mathematical model for the study of the nonlinear torsional vibrations of a one-stage transmission gear system with backlash is presented. Four different techniques based on discretization method, perturbation method, Ritz method, and stepwise time-integration method modelled with Simulink are compared in terms of time and frequency response. It has been demonstrated that although all the investigated methods are accurate and computationally effective for finding the main spectral contribution, only discretization and step-wise time-integration methods are able to identify the other frequency components.

A hybrid modelling technique for the simulation of the torsional vibration of vehicle driveline systems is proposed in [8]. More specifically, the driveline is modelled partially as a lumped system and partially as a distributed parameter system: the authors show that hybrid modelling allows identifying the high frequency components associated with clonk, while a simple lumped model cannot.

In [9], an experimental activity for the analysis of clonk phenomenon is shown: torsional impulses are applied through a torque preload system to a drivetrain rig in order to excite high frequency clonk modes. Calibrated accelerometers are located in various positions along the driveline in order to record tangential acceleration. A typical spectral composition for the driveshaft is reported, indicating high frequency contents in the range 1.5–5 kHz.

In [10] the experimental and analytical methodologies for characterizing the torsional dynamic behaviour of an Automated Manual Transmission (AMT) and a DMF are discussed. The effects of changing the gear ratio of the AMT in terms of Frequency Response Function (FRF) compliance are shown from the measures and from the simulation results of the proposed model.

Other authors [11] propose a method to calculate the various time-varying parameters: transmission error, length of contact line, meshing stiffness, meshing damping coefficient, input and output torque, dynamic meshing force, and dynamic friction force.

In case of transmissions with Hooke's joints, as common in many automotive systems, [12] proposes a torsional vibration mathematical model of the transmission shaft, driving gear, and driven gear based on lumped masses and the main reducer system assembly. The influence of the angle between transmission shafts and intermediate support stiffness on the vibration and noise of the main reducer is obtained and verified experimentally.

With regard to the experimental approach, the novel approach proposed in [13] to simulate the actual working condition when testing dynamic stiffness is worth citing. In experimental modal analysis of powertrain mounting systems, the method of traditional impact hammer testing may produce large error and the identification results of modal parameters are not reliable, while identification using the method of operational modal analysis allows obtaining more accurate and reliable results, which are consistent with the actual working condition.

In the first part of the paper, the authors describe the transmission test rig for torsional vibration analysis available at the Politecnico di Torino, discussing its potentialities. In particular, they address some aspects of the interaction between the electric motors control and the mechanical parts of the test rig.

The 4-dof lumped parameter model of the tested transmission proposed in [14] has been improved: here the authors propose a 5-dof model, aiming at analysing the torsional behaviour up to higher frequencies. The modal shapes and natural frequencies of the modelled system are discussed and the FRF matrix is derived.

The analysis of the simulation results highlights the effects of the electric motors control tuning and of some physical parameters on the system torsional behaviour.

The last part of the paper draws some considerations on the postprocessing method to estimate the Frequency Response Functions from the experimental data: the comparison between simulated and experimental results is presented. Moreover, some effects of the nonlinearities associated with the mean value of the excitations are shown and discussed. Finally the influence of the selected gear ratio on the experimental frequency response is presented.

2. Transmission Test Bench

Figure 1 shows the transmission test bench located in the Mechanics Laboratory at the Politecnico di Torino. Its main components are two electric motors (M1 and M2) and two transmission systems for passenger cars with locked differentials, that is, a Dual Clutch Transmission (DCT) and a Manual Transmission (MT).

As visible in Figure 2, both the DCT and MT gearboxes are used to amplify the torque delivered by the electric motors connected to the respective input shafts. The two output shafts SA1 and SA2 are connected through a brake disk D.

The test bench is equipped with many sensors (encoders and inductive pick-ups to measure speed, torque, and temperature transducers) aiming at monitoring the actual dynamic state of the transmission system. For torsional vibration analysis, the most relevant sensors are

(i) two torque-meters (T1 and T2 in Figure 2), measuring the torque provided by the two electric motors;

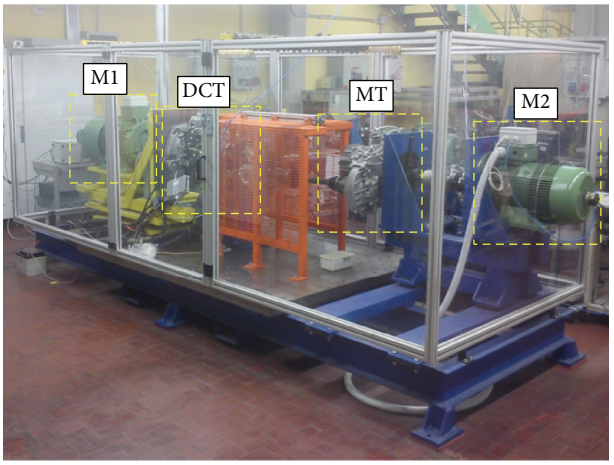

Figure 1: Transmission test bench at the Politecnico di Torino.

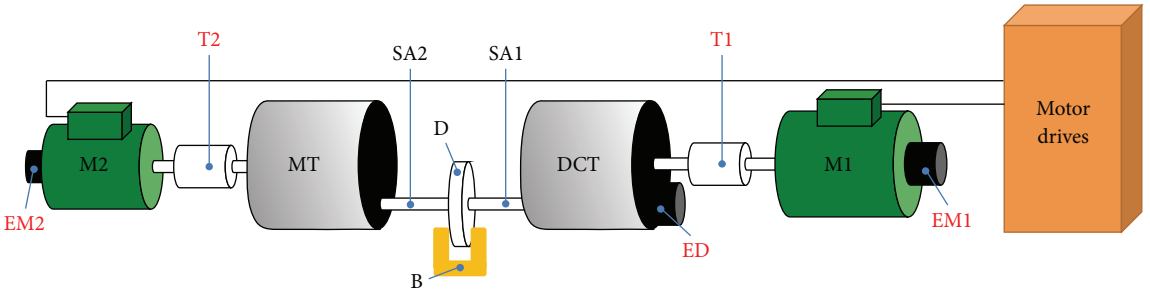

Figure 2: Layout of the transmission test bench: electric motors (M1, M2), speed sensors (encoders EM1, EM2, and ED), torque sensors (T1, T2), disk (D), brake (B), and output half shafts (SA1, SA2).

(ii) three incremental encoders (see Table 1 for the resolutions): EM1 and EM2 measure the angular speed of the two motors while ED measures the speed of the DCT differential.

The test bench is conceived as a Hardware-in-the-Loop (HiL) system aiming at reproducing typical manoeuvres representative of the real usage of a gearbox on a passenger car. This goal is achieved through the implementation of a simulation model running and exchanging information in real time with the physical sensors and actuators of the test bench. Some examples of test benches sharing a similar HiL technology are reported in [15–17].

In Figure 1, from left to right, the following components are visible:

(i) M1: a three-phase induction electric motor used to simulate the prime mover of the vehicle, for example, the Internal Combustion Engine.

(ii) DCT: a 6-speed dry Dual Clutch Transmission (see, e.g., [18] for the kinematic and dynamic behaviour of this transmission).

(iii) MT: a 6-speed Manual Transmission.

Table 1: Data of the encoders.

Encoder location	Pulses per revolution
EM1	1024
ED	9000
EM2	4096

(iv) M2: a second three-phase induction electric motor that simulates the vehicle load, that is, the aerodynamic and rolling resistance, the road slope, and the vehicle inertial effects.

It is worth noting that the good controllability in terms of torque and speed of both electric motors allows generating standard (e.g., step, sine wave, or chirp) and custom excitations. Moreover, speed sensors along the transmission allow monitoring the dynamical system response.

Consequently, the torsional vibrations of the transmission system can be investigated: the rest of the paper focuses on this aspect.

3. System Model

The linearized lumped parameter model used to study the torsional behaviour of the dynamic system is depicted in

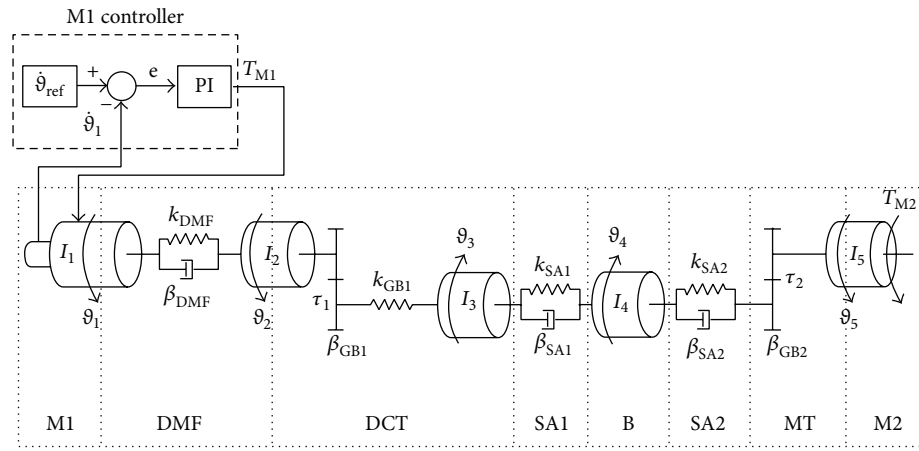

Figure 3: Torsional model of the test bench.

Table 2: Numerical values of the model parameters.

Parameter	Value	Unit
I_1, I_2, I_3, I_4, I_5	0.19, 0.14, 0.12, 0.18, 0.065	kgm^2
$k_{DMF}, k_{GB1}, k_{SA1}, k_{SA2}$	0.46, 96, 12, 14.9	kNm/rad
$\beta_1, \beta_2, \beta_3, \beta_4, \beta_5$	0.2, 2, 0.02, 0.34, 0.2	Nms/rad
$\beta_{SA1}, \beta_{SA2}, \beta_{GB1}, \beta_{GB2}$	0.1, 0.1, 0, 4	Nms/rad
k_P, k_I	1.75, 15	Nms/rad, Nm/rad
τ_1 τ_2	5.91 (3rd gear), 4.03 (4th gear)	—

Figure 3. The numerical values of the parameters used for the simulation are shown in Table 2.

The model considers the interaction between the mechanical parts and the speed/torque controllers realized by the electric motor drives.

3.1. Electric Motors Control. Electric motor M1 is speed-controlled, while motor M2 is torque-controlled. A constant speed is the set point for the M1 controller, while motor M2 provides an almost harmonic torque excitation, with a frequency varying with time in the desired frequency range.

The speed control of the electric motor M1 is implemented through a Proportional-Integral (PI) algorithm:

$$T_{M1} = k_P\left(\dot{\theta}_{ref} - \dot{\theta}_1\right) + k_I \int \left(\dot{\theta}_{ref} - \dot{\theta}_1\right) dt, \quad (1)$$

where k_P and k_I are the proportional and integral gains, respectively.

Under the assumption that the speed set point is constant ($\dot{\theta}_{ref}$ = const), the former equation can be written in the form

$$T_{M1} = \dot{\theta}_{ref}\left(k_P + k_I \cdot t\right) - k_I\theta_1 - k_P\dot{\theta}_1. \quad (2)$$

Equation (2) shows that the integral gain acts as a torsional stiffness, that is, the elastic term being $k_I\theta_1$, while the proportional gain acts as a viscous damping, the viscous term being $k_P\dot{\theta}_1$.

The torque applied by electric motor M2 is a different matter. In fact, considering small oscillations around an equilibrium point and neglecting the constant torque that the motors have to deliver to guarantee that steady-state condition, it is not necessary to show explicitly the torque applied by the electric motor M2. A harmonic excitation applied to one of the inertias of the system, the one having moment of inertia I_5 in this case, is implicit in the receptance method [19].

3.2. Torsional System Dynamics. A 5-dof torsional system is used to describe the dynamic behaviour of the mechanical system under test. The DCT gearbox is modelled considering the gear ratio τ_1 of the actual gear (defined as the ratio between input and output speed), an overall torsional stiffness k_{GB1} of the active transmission path, and two moments of inertia, that is, part of inertia I_2 and inertia I_3 mainly related to the differential.

For the Dual Mass Flywheel of the DCT installed on the test bed, a low stiffness spring k_{DMF} and a viscous damper with damping coefficient β_{DMF} are introduced in the model. The moment of inertia of the first DMF mass is added to the M1 rotor inertia just before the spring and damper element, while the second mass is added to the equivalent inertia of the DCT (except its differential) evaluated at its input shaft.

The second gearbox named MT is modelled as simple gear pairs characterised by the actual gear ratio τ_2 with unitary efficiency. The MT total moment of inertia is reflected to the input shaft and constitutes a part of inertia I_5.

The two half shafts SA1 and SA2 are modelled as elements possessing torsional elastic and damping characteristics.

The generalized coordinates are the angular positions of each flywheel composing the system: $q = \{\theta_1 \ \theta_2 \ \theta_3 \ \theta_4 \ \theta_5\}^T$.

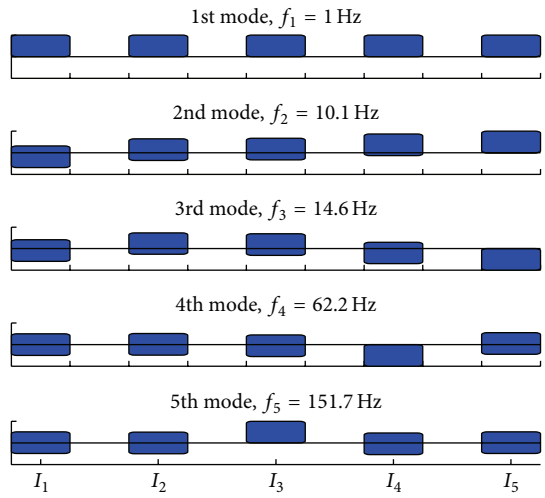

FIGURE 4: Natural frequencies and mode shapes computed from the simulation model.

The equations of motion of the torsional system depicted in Figure 3 are

$$\begin{aligned}
&I_1\ddot{\theta}_1 + k_{\mathrm{DMF}}\left(\theta_1 - \theta_2\right) + \beta_{\mathrm{DMF}}\left(\dot{\theta}_1 - \dot{\theta}_2\right) + \beta_1\dot{\theta}_1 \\
&\quad + T_{\mathrm{M1}} = 0, \\
&I_2\ddot{\theta}_2 + \left(\beta_2 + \frac{\beta_{\mathrm{GB1}}}{\tau_1^2}\right)\dot{\theta}_2 - k_{\mathrm{DMF}}\left(\theta_1 - \theta_2\right) \\
&\quad - \beta_{\mathrm{DMF}}\left(\dot{\theta}_1 - \dot{\theta}_2\right) - \frac{k_{\mathrm{GB1}}}{\tau_1}\left(\theta_3 - \frac{\theta_2}{\tau_1}\right) = 0, \\
&I_3\ddot{\theta}_3 + \beta_3\dot{\theta}_3 + k_{\mathrm{GB1}}\left(\theta_3 - \frac{\theta_2}{\tau_1}\right) + k_{\mathrm{SA1}}\left(\theta_3 - \theta_4\right) \\
&\quad + \beta_{\mathrm{SA1}}\left(\dot{\theta}_3 - \dot{\theta}_4\right) = 0, \\
&I_4\ddot{\theta}_4 + \beta_4\dot{\theta}_4 + k_{\mathrm{SA2}}\left(\theta_4 - \frac{\theta_5}{\tau_2}\right) + \beta_{\mathrm{SA2}}\left(\dot{\theta}_4 - \frac{\dot{\theta}_5}{\tau_2}\right) \\
&\quad + k_{\mathrm{SA1}}\left(\theta_4 - \theta_3\right) + \beta_{\mathrm{SA1}}\left(\dot{\theta}_4 - \dot{\theta}_3\right) = 0, \\
&I_5\ddot{\theta}_5 + \left(\beta_5 + \frac{\beta_{\mathrm{GB2}}}{\tau_2^2}\right)\dot{\theta}_5 - \frac{k_{\mathrm{SA2}}}{\tau_2}\left(\theta_4 - \frac{\theta_5}{\tau_2}\right) \\
&\quad - \frac{\beta_{\mathrm{SA2}}}{\tau_2}\left(\dot{\theta}_4 - \frac{\dot{\theta}_5}{\tau_2}\right) = 0
\end{aligned} \tag{3}$$

which can be cast in matrix form

$$\begin{aligned}
&[M]\{\ddot{q}\} + [B]\{\dot{q}\} + [K]\{q\} \\
&\quad = \{1 \;\; 0 \;\; 0 \;\; 0 \;\; 0\}^T \dot{\theta}_{\mathrm{ref},1}\left(k_P + k_I t\right),
\end{aligned} \tag{4}$$

where the mass, damping, and stiffness matrices are reported in the appendix.

3.3. Natural Frequencies and Mode Shapes. By solving the eigenvalue problem associated with the undamped system, that is,

$$\left([K] - \omega_i^{\,2}[M]\right)\{\psi\}_i = \{0\}, \quad i = 1, \ldots, 5, \tag{5}$$

it is possible to compute the natural frequencies $f_i = \omega_i/2\pi$ and the associated modal shapes, described by the natural modes or modal vectors $\{\psi\}_i$.

The mode shapes are normalized so that the modulus of the maximum element of each eigenvector is unitary.

Moreover, due to the presence of two gear ratios, that is, the transmission ratio of the two gearboxes, it is convenient to show the eigenvectors referred to the same shaft, for example, the shaft of the electric motor M1. As an example, the rth eigenvector is scaled as follows:

$$\{\psi\}_{r,\mathrm{M1}} = \left\{\psi_1, \psi_2, \tau_1\psi_3, \tau_1\psi_4, \frac{\tau_1}{\tau_2}\psi_5\right\}_r^T. \tag{6}$$

Figure 4 shows the natural frequency and the mode shape referred to M1 shaft for each of the five vibration modes.

The first low frequency mode (≈1 Hz) is almost a rigid body mode and is primarily associated with the electric motor speed controller. Increasing the integral gain k_I of the PI controller determines an increase of the first resonance frequency of the system, while increasing the proportional gain k_P raises the damping factor relative to the first mode (Figures 5 and 6).

The second mode is the first real torsional mode of the system. The 2nd and 3rd natural frequencies are very close to each other (approximately 10 Hz for the second and 15 Hz for the third); hence their individual effects combine to give rise to a single peak in the frequency response at an intermediate frequency between the two, that is, 12.5 Hz. A larger inertia of the electric motor M1 (I_1) reduces that frequency, while a bigger mass of the second flywheel (I_2) amplifies the peak

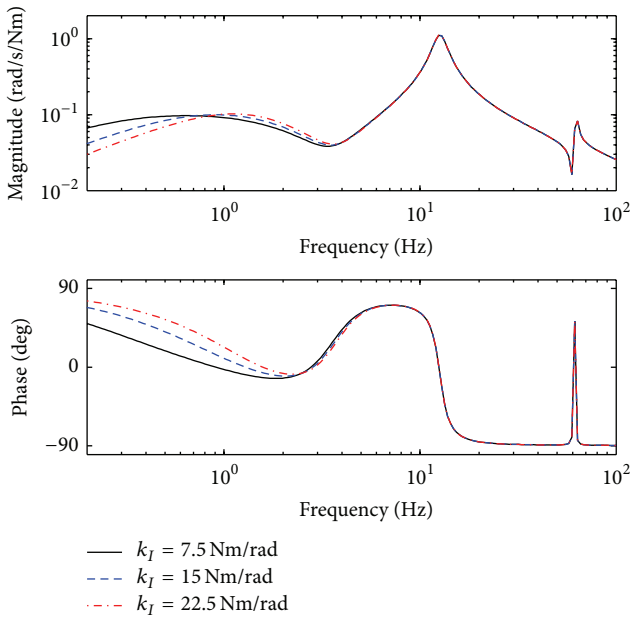

FIGURE 5: Sensitivity analysis results: effect of the integral gain of the PI speed controller on the FRF $\dot{\theta}_5/T_5$.

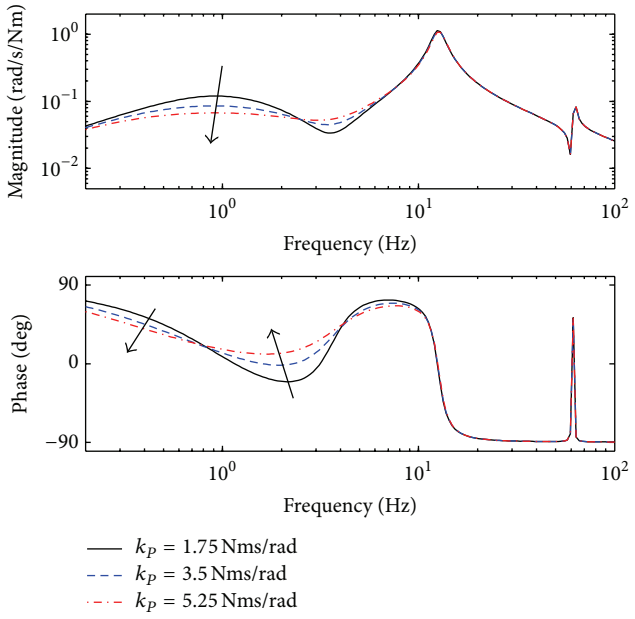

FIGURE 6: Sensitivity analysis: effect of the proportional gain of the PI speed controller on the FRF $\dot{\theta}_5/T_5$.

amplitude. Increasing the half-shaft stiffness shifts the peak to higher frequencies. If the DMF damping is small enough, there are two separate peaks; increasing damping initially flattens the two peaks and then produces an increase of the single peak amplitude (Figure 7).

The last two high frequency modes show a very similar characteristic: in both cases a single inertia vibrates with respect to the remaining part of the driveline, which stays practically stationary. The 4th mode is at about 62 Hz and

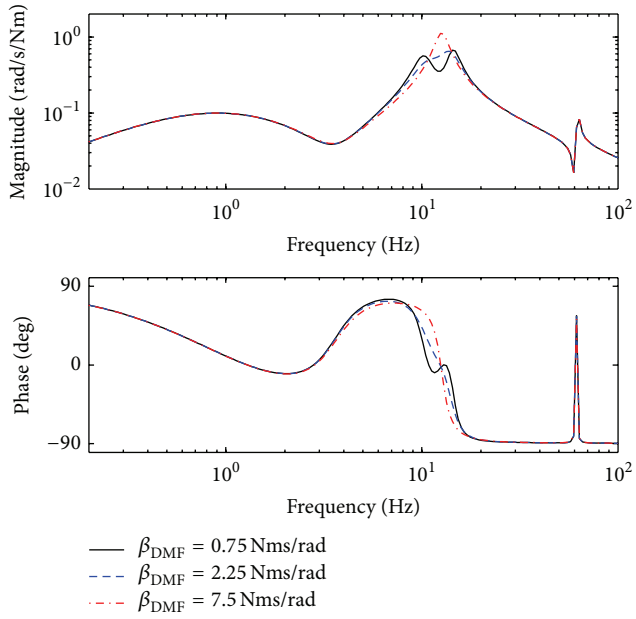

FIGURE 7: Sensitivity analysis: effect of the DMF damping coefficient on the FRF $\dot{\theta}_5/T_5$.

involves mainly the brake disk inertia I_4, while the 5th mode (152 Hz) is due to the vibration of the DCT differential I_3. Therefore, the dynamic behaviour of the system and its sensitivity to the parameters in the neighbourhood of the correspondent natural frequency are similar to those of a 1-dof system. As an example, the equivalent 1-dof system for the 4th mode is composed of inertia I_4, stiffness $k_{SA1} + k_{SA2}$, and damping β_3.

3.4. Frequency Response Functions. The response of a viscously damped n-dof system to a harmonic excitation can be calculated by means of the receptance matrix $\alpha(\Omega)$, relating the displacement of each degree of freedom θ_i to the excitation T as a function of frequency:

$$\{\theta_0\} = [\alpha(\Omega)]\{T_0\}, \tag{7}$$

where $\{T_0\}$ is a real vector of constant amplitudes while $\{\theta_0\}$ is a complex vector. Matrix $\alpha(\Omega)$ can be calculated as the inverse of the dynamic stiffness matrix; that is,

$$[\alpha(\Omega)] = \left[K_{dyn}\right]^{-1} = \left([K] + j\Omega[B] - \Omega^2[M]\right)^{-1}. \tag{8}$$

The measures on the test bench are angular speeds and torques; hence the FRFs to be computed from the model are the ratios between these two quantities, called mobility functions [19].

If motion is harmonic, the relationship between speed and angular position amplitudes is

$$\dot{\theta}_0 = j\Omega\theta_0 \tag{9}$$

so that

$$\left\{\dot{\theta}_0\right\} = j\Omega[\alpha(\Omega)]\{T_0\}. \tag{10}$$

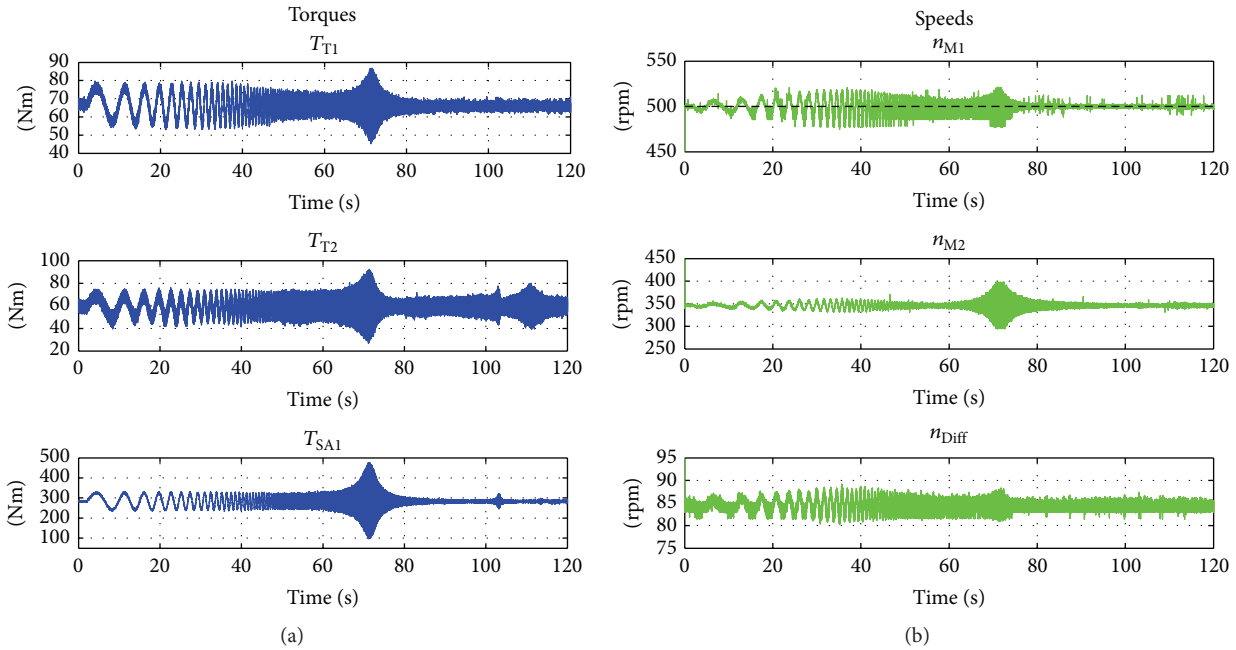

FIGURE 8: Time histories of the torques (a) and the speeds (b) during a chirp test.

More specifically, the harmonic torque T_5 is applied from electric motor M2 to the 5th inertia of the system; consequently the only element of $\{T_0\}$ different from zero is the fifth one ($\{T_0\} = T_0\{0\ 0\ 0\ 0\ 1\}^T$) so that the set of equations representing the frequency response of each degree of freedom contains only the fifth column of the receptance matrix:

$$\frac{\begin{Bmatrix}\dot{\theta}_1\\ \dot{\theta}_2\\ \dot{\theta}_3\\ \dot{\theta}_4\\ \dot{\theta}_5\end{Bmatrix}}{T_5} = j\Omega \begin{Bmatrix}\alpha_{1,5}(\Omega)\\ \alpha_{2,5}(\Omega)\\ \alpha_{3,5}(\Omega)\\ \alpha_{4,5}(\Omega)\\ \alpha_{5,5}(\Omega)\end{Bmatrix}. \tag{11}$$

As explained in [10], the torque measured on the bench is not directly the excitation since the sensor T2 is mounted on the output shaft, that is, downstream the electric motor inertia and the bearing damping. Consequently the following equation must be considered:

$$\frac{\dot{\vartheta}_i}{T_{T2}} = \left(\frac{\dot{\vartheta}_i}{T_5}\right)\cdot\left(1 + I_{M2}\Omega^2\frac{\vartheta_5}{T_5} - c_5 j\Omega\frac{\vartheta_5}{T_5}\right)^{-1}. \tag{12}$$

Alternatively, the mechanical system upstream of the measuring point must be neglected in the model; that is, the model of the system must not take into account the mechanical model of the electric motor that excites the system.

4. Experimental Tests

During a torsional vibration test, one electric motor (e.g., M2) produces a sinusoidal torque having almost constant amplitude and continuously variable frequency (torque control is enabled for this motor), while the second motor (M1) tries to keep the speed of its shaft constant (closed-loop speed control mode enabled).

It should be noted that, before the torsional excitation starts, the system must be brought to a steady-state condition, that is, constant speed and torque, where the behaviour of the system can be linearized. A torque offset must be therefore constantly applied and added to the harmonic trend during the test, in order to have approximately constant system parameters, for example, no appreciable stiffness variations, and no crossing of the line of zero torque to avoid the nonlinear phenomena associated with load reversal (impact between rotating components due to backlash).

Time histories of the torques applied by the two electric motors are measured and collected together with the angular speeds in three points of the transmission line (Figure 8).

The sinusoidal torque set point is

$$T_{\text{ref},5} = T_0 + \sin\left(2\pi f(t)\, t\right) \tag{13}$$

with constant amplitude and frequency f varying as a power function of time (logarithmic chirp); that is,

$$f(t) = f_0 \cdot \left(\frac{f_1}{f_0}\right)^{t/t_1}. \tag{14}$$

The logarithmic trend can be clearly seen in Figure 9, showing the spectrogram of the torque measured by sensor T2. A 12th-order related vibration, probably due to the torque generation system of the electric machine, is also visible in the same plot.

A postprocessing tool based on the H_1 estimator (see, e.g., [10, 20] for details) applied to the acquired data allows

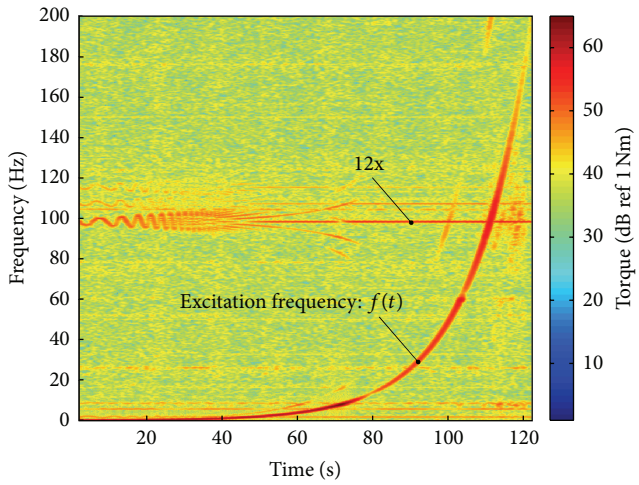

FIGURE 9: Time-frequency spectrogram of torque T_{M2}.

obtaining the transfer functions between the input torque, applied by the electric motor M2, and the rotational speeds.

Even if an external load is applied by both electric motors, a single-input multiple-output (SIMO) approach can be used to analyse the dynamic behaviour of the system. The closed-loop speed controller of the electric motor must become part of the system under test and so its mathematical description is included in the model.

Figures 10–12 show the FRFs estimated from the measures together with the coherence functions. Since the excitation for the dynamic system is generated by electric motor M2, the amplitude of the response $\dot{\theta}_5$ is high enough to be measured accurately by the encoder up to more than 150 Hz. Conversely, the lower amplitude of oscillation of the other electric motor M1 due also to the lower sensor resolution limits the range of reliability of $\dot{\theta}_1/T_5$ to 20 Hz.

The sensors used to measure the angular velocity of the three instrumented shafts are incremental encoders having different resolutions as shown in Table 1. High-resolution encoders allow extending the frequency analysis towards higher frequencies. As an example, even if the amplitude of the oscillation at the differential output is low (see Figure 12), the FRF shows a clear trend up to more than 150 Hz.

Under the assumption that the system under test is linear (at least in the neighborhood of the equilibrium point around which the system vibrates) and time-invariant, the estimation of a FRF from experimental data can be performed by calculating the Power Spectral Density (PSD) and the Cross-Power Spectral Density (CSD).

The method generally used for computing these two quantities is Welch's method [21]: it allows better noise reduction in comparison with the standard periodogram spectrum estimating method or Bartlett's method that averages the estimates derived from contiguous nonoverlapping portions of the original signal.

Welch's method instead is based on time averaging over short, windowed periodograms, applied to overlapping segments.

The PSD estimate using Welch's method is

$$\widehat{G}_{xx}(k) = \frac{S_P}{M}\sum_{m=1}^{M}\left|X_{w,m}(k)\right|^2, \quad k = 1, 2, \ldots, \frac{N}{2}, \tag{15}$$

where hat symbol $\widehat{\ }$ denotes the estimated functions, M is the number of segments having length N, S_P is a scaling factor, and $X_{w,m}(k)$ is the Discrete Fourier Transform (DFT) of the mth windowed segment; that is,

$$X_{w,m}(k) = \mathrm{DFT}\left[x_m(n)\cdot w(n)\right], \tag{16}$$

where $x_m(n)$ is the mth data segment, $w(n)$ is the window applied to each segment, and n is the identifier of each sample in the data segment. The time blocks in which the total time histories of the two measures are subdivided are overlapped, thus decreasing the random error of the estimate.

As stated in [21], when calculating PSD and CSD the random error is influenced by windowing and overlap processing; more specifically with increasing overlap percentage at first we get a substantial reduction in the variance for increasing overlap, while, above a particular overlap percentage, the additional gain is very small. Since the experimentally evaluated FRF using H_1 estimator is the ratio between CSD and PSD, the same concepts apply also for the FRF variance, as illustrated in Figure 13, where the effect of the percentage of overlap used during the averaging process on the quality of the estimated FRF is shown.

The influence of some nonlinearities of the system is shown in Figure 14, plotting the modulus of the FRF between the desired torque $T_{\mathrm{ref},5}$ and the actual value $T_{\mathrm{fb},5}$ measured through torque meter T2 for three different values of the mean value of M2 torque: an increase of the mean value causes larger amplitude of the FRF.

Finally, Figure 15 shows the influence of different gear ratios on the FRF. The most relevant consequences are a frequency shift of the first FRF peak and the increase of the peaks amplitude.

4.1. Model Order Selection. The model development was driven, for simplicity issues, by the will to use the minimum number of dof necessary to describe the system dynamics in the frequency range of interest.

It must be observed that since every mechanical system has distributed properties (inertial, elastic, and dissipative), the choice of the position where the inertias should be lumped is not always obvious, especially if the frequency range of interest increases. As an example, the first modelling attempt was to use only 4 dof: the DCT was simply modelled as done for MT. Comparing experimental and simulated FRFs, significant differences in phase and the lack of a peak in the magnitude at about 150 Hz were observed, as reported in Figure 16: the additional dof in correspondence of the differential of the DCT allows increasing the accuracy of the estimate.

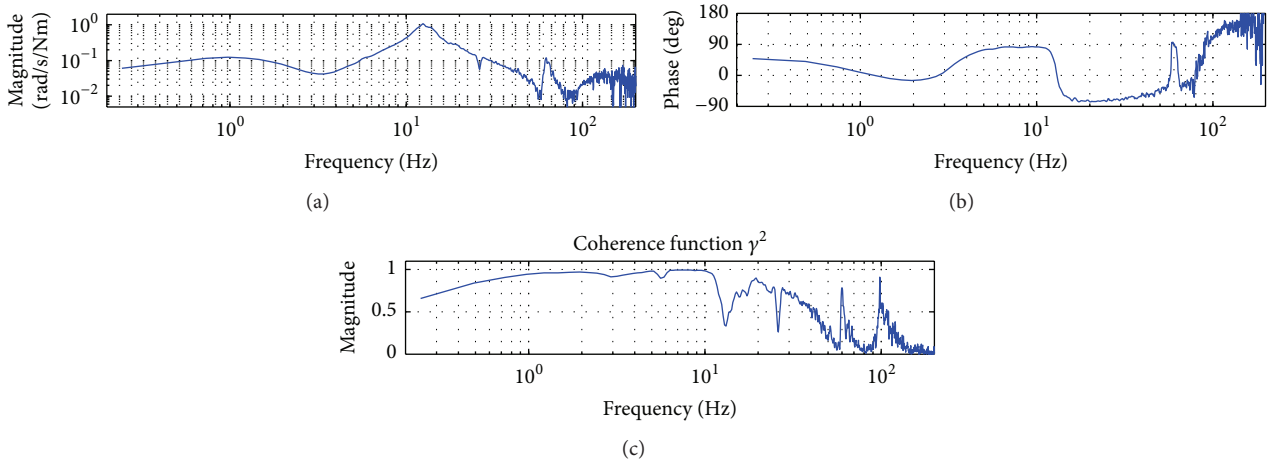

FIGURE 10: FRF $\dot{\theta}_5/T_5$: modulus (a), phase (b), and coherence function (c).

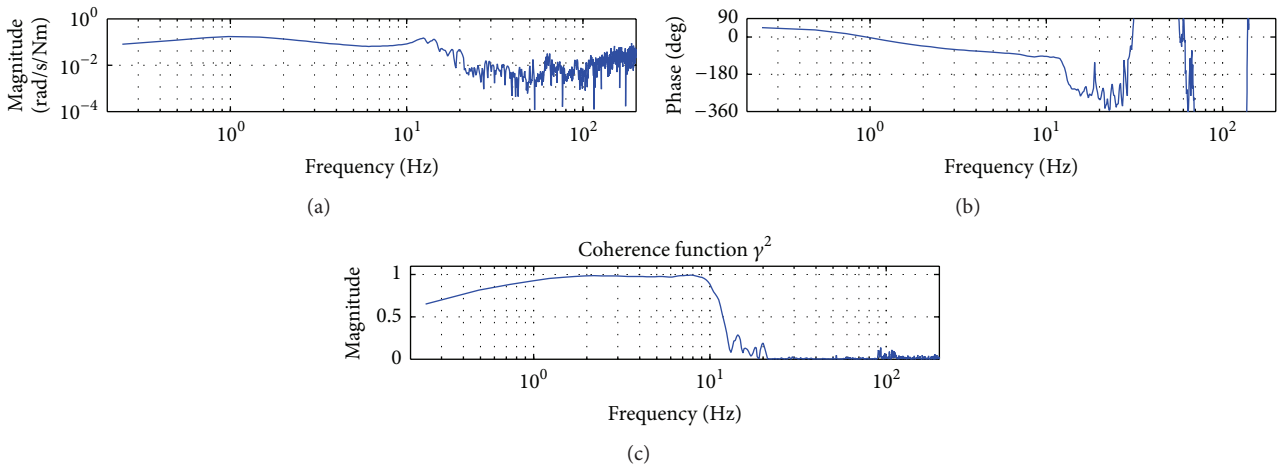

FIGURE 11: FRF $\dot{\theta}_1/T_5$: modulus (a), phase (b), and coherence function (c).

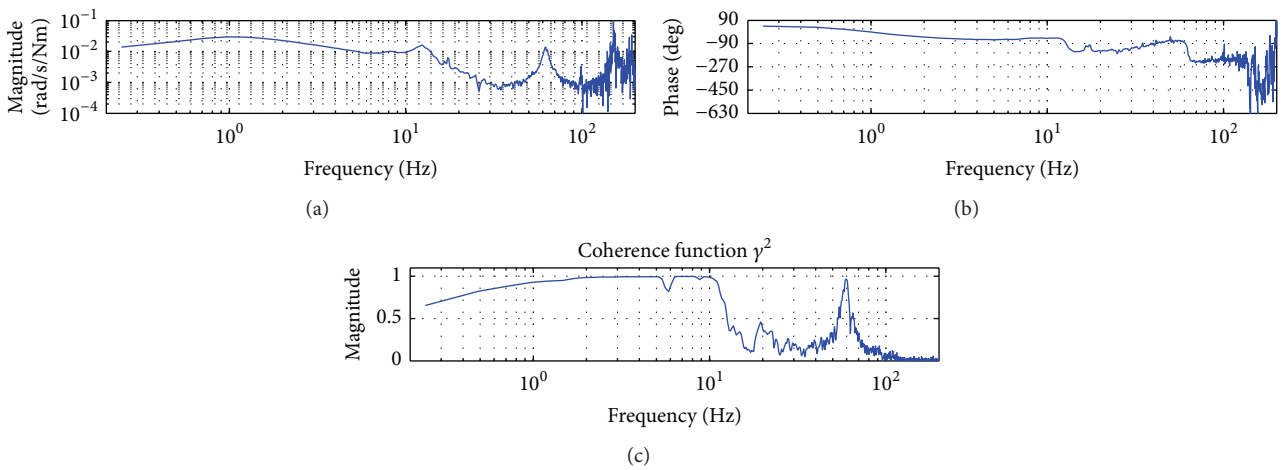

FIGURE 12: FRF $\dot{\theta}_3/T_5$: modulus (a), phase (b), and coherence function (c).

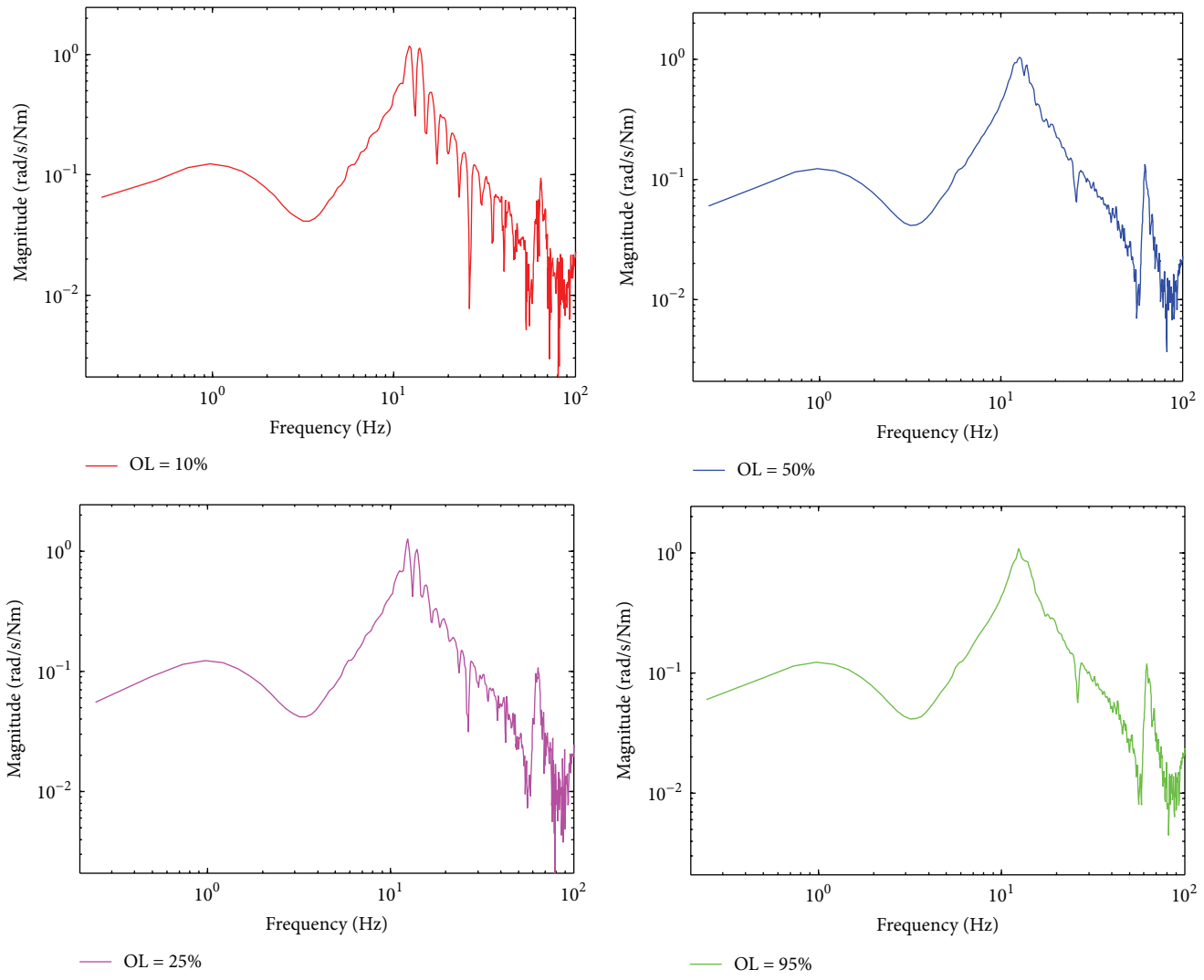

FIGURE 13: Overlap effect on the estimated FRF $\dot{\theta}_5/T_5$ with Hamming window (windows length 2.5 s).

5. Model Validation

The plots reported in Figures 17–19 show the comparison between the simulated FRF, calculated numerically by evaluating (11), and the FRF estimated from the experimental results, that is, using the measures of torque and speed on the test rig.

The correspondence between simulated and experimental curves is excellent in case of FRFs $\dot{\theta}_5/T_5$ and $\dot{\theta}_3/T_5$ in both modulus and phase. Similarly, Figure 18 (FRF $\dot{\theta}_1/T_5$) shows a fairly good correspondence for both modulus and phase up to the limit of reliability of the experimental data (20 Hz). The frequency and amplitude of the resonance peaks are well captured by the model.

5.1. Results Analysis. A quantitative comparison between the measured and simulated FRFs is given in Table 3 (it must be underlined that results for FRFs $\dot{\theta}_2/T_5$ and $\dot{\theta}_4/T_5$ are not shown due to lack of experimental measures). The root mean square (RMS) of the difference between the experimental and the simulated magnitude and phase of the FRFs is the index chosen to evaluate the model accuracy.

TABLE 3: Estimation error for FRFs $\dot{\theta}_1/T_5$, $\dot{\theta}_3/T_5$, and $\dot{\theta}_5/T_5$.

FRF	f_{max} [Hz]	RMS (exp-sim) Magnitude [rad/s/Nm]	RMS (exp-sim) Phase [°]
$\dot{\theta}_1/T_5$	200	1,35$E-02$	533
	21	1,40$E-02$	30
$\dot{\theta}_3/T_5$	200	3,00$E-03$	45
$\dot{\theta}_5/T_5$	200	3,20$E-02$	81
	70	3,40$E-02$	29

The results concerning the first FRF ($\dot{\theta}_1/T_5$) are affected by a relevant phase RMS difference if the whole frequency

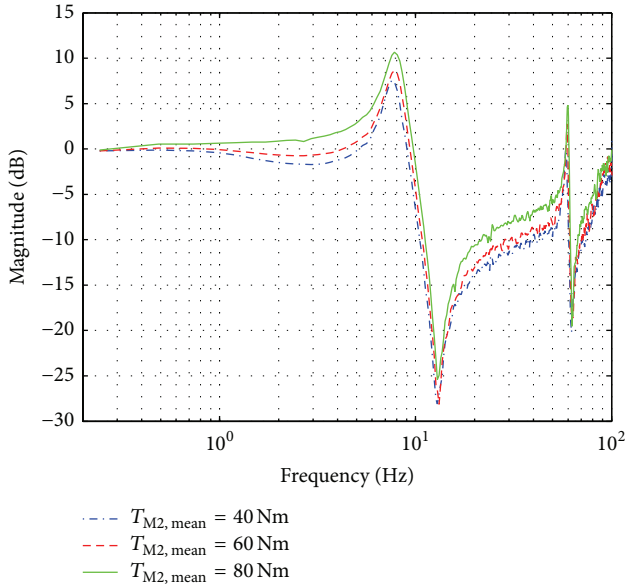

FIGURE 14: Effect of the mean value on the modulus of the FRF $T_{fb,5}/T_{ref,5}$.

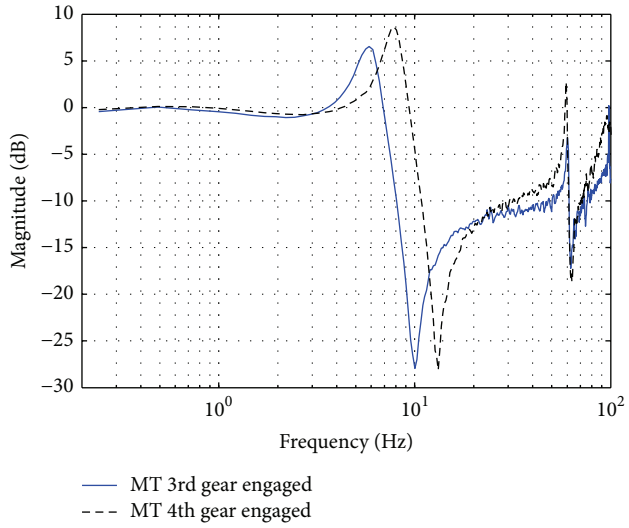

FIGURE 15: Effect of the gear ratio on the modulus of the FRF $T_{fb,5}/T_{ref,5}$.

range, that is, up to a maximum frequency f_{max} = 200 Hz, is considered. This is due to the low resolution of encoder M1 with respect to the angular displacement to measure; therefore the error at high frequencies is mainly attributable to errors in the experimental measures rather than to the model, as also confirmed by the coherence function that drops to zero very quickly after 21 Hz (see Figure 11). Limiting the maximum frequency to 21 Hz, that is, up to the value for which the experimental data are reliable, the phase error becomes significantly smaller.

FRF $\dot{\theta}_3/T_5$ is very well estimated in the whole frequency range, the shapes of the experimental magnitude and phase

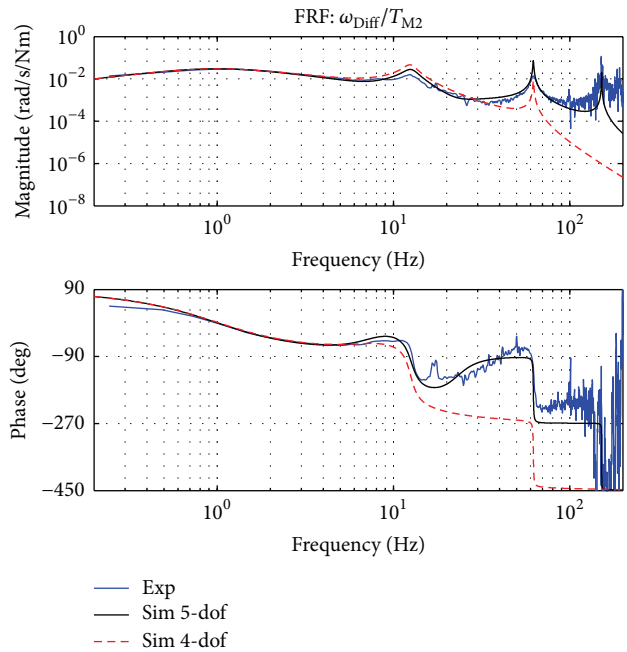

FIGURE 16: Tuning of the model order with the experimental FRF.

trends are well captured by the model, as visible in Figure 19, and the accuracy of the measure is also adequate up to 200 Hz due to the high encoder resolution, thus resulting in small RMS errors for both magnitude and phase.

Two RMS values are calculated for FRF $\dot{\theta}_5/T_5$: the first one is on the whole frequency range, while the second is limited to 70 Hz. As visible also qualitatively from Figure 17, the accuracy of the estimation decreases significantly immediately after the third peak in magnitude. Probably an additional degree of freedom is needed in order to extend the validity of the model up to 200 Hz also for this FRF: further investigation is required in order to solve this issue.

6. Conclusions

The torsional vibrations of a transmission system mounted on a test rig have been investigated and a reliable lumped parameter model has been developed. A sensitivity analysis highlighting the effect of the electric motors control tuning and other model parameters on the global torsional behaviour is presented.

The first highly damped torsional mode of the transmission system (≈1 Hz) is almost a rigid body mode and it is primarily associated with the electric motor speed controller.

The second mode is the first real torsional mode of the system. The 2nd and 3rd natural frequencies are very close to each other; hence their individual effects combine to give rise to a single peak in the FRFs at about 12.5 Hz.

The 4th and 5th modes represent the vibrations of the brake disk (inertia I_4) and of the DCT differential (inertia

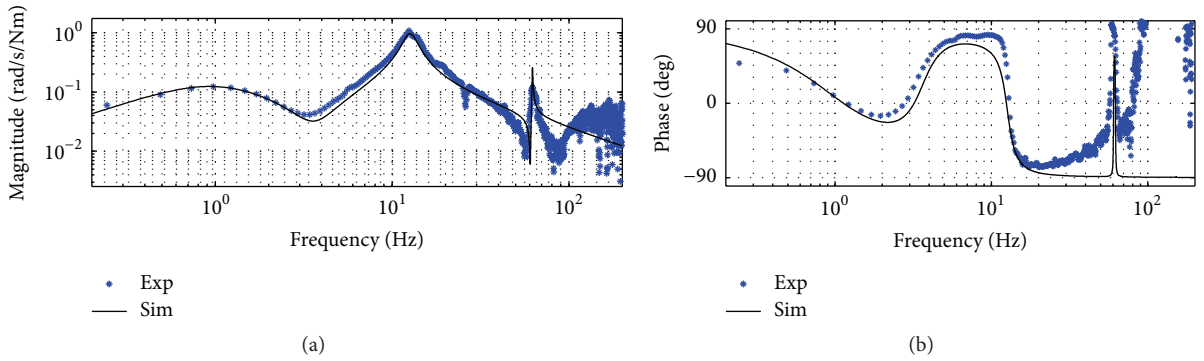

FIGURE 17: FRF of $\dot{\theta}_5/T_5$: modulus (a) and phase (b).

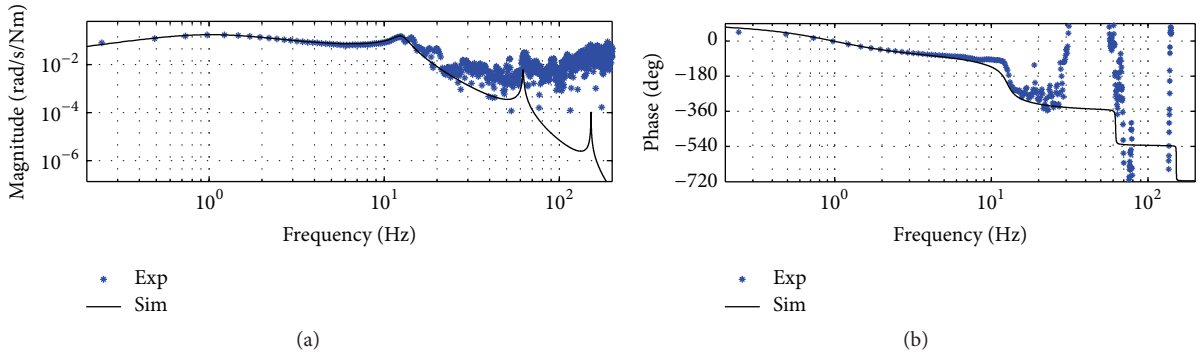

FIGURE 18: FRF $\dot{\theta}_1/T_5$: modulus (a) and phase (b).

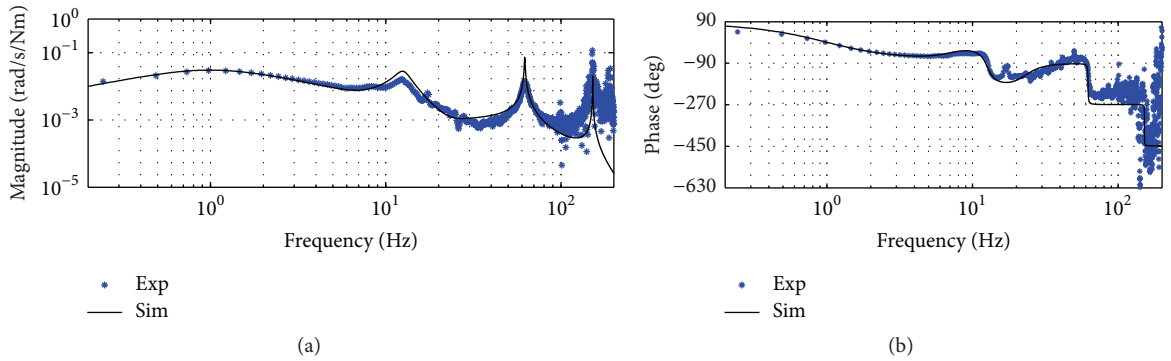

FIGURE 19: FRF $\dot{\theta}_3/T_5$: modulus (a) and phase (b).

I_3), with respect to the remaining part of the driveline that remains practically stationary.

Comparing experimental and simulated results, the paper shows where to concentrate the model parameters of the transmission system in order to obtain an accurate estimation of the experimental frequency response. Adding a dof representing the DCT differential inertia results in an additional peak in the frequency response and shifts up the phase at high frequencies according to the experimental results.

The comparison with the results obtainable with models using a smaller number of degrees of freedom shows that five dof is an appropriate choice to describe the linear torsional system behaviour up to a frequency of 200 Hz.

The nonlinear behaviour of the system under test is highlighted through specific measurements: an increase of the mean torque value applied during the tests causes larger magnitudes of the FRF. Also the influence of the actual gear of the MT has been experimentally investigated: the most relevant consequence is a frequency shift of a FRF peak.

Appendix

System Matrices

Mass, stiffness, and damping matrices are as follows:

$$[M] = \operatorname{diag}\left(I_1, I_2, I_3, I_4, I_5\right),$$

$$[B] = \begin{bmatrix} \beta_{\mathrm{DMF}} + \beta_1 + k_P & -\beta_{\mathrm{DMF}} & 0 & 0 & 0 \\ -\beta_{\mathrm{DMF}} & \beta_{\mathrm{DMF}} + \beta_2 + \dfrac{\beta_{\mathrm{GB1}}}{\tau_1^2} & 0 & 0 & 0 \\ 0 & 0 & \beta_3 + \beta_{\mathrm{SA1}} & -\beta_{\mathrm{SA1}} & 0 \\ 0 & 0 & -\beta_{\mathrm{SA1}} & \beta_{\mathrm{SA1}} + \beta_{\mathrm{SA2}} + \beta_4 & -\dfrac{\beta_{\mathrm{SA2}}}{\tau_2} \\ 0 & 0 & 0 & -\dfrac{\beta_{\mathrm{SA2}}}{\tau_2} & \beta_5 + \dfrac{\beta_{\mathrm{GB2}}}{\tau_2^2} \end{bmatrix},$$

$$[K] = \begin{bmatrix} k_{\mathrm{DMF}} + k_I & -k_{\mathrm{DMF}} & 0 & 0 & 0 \\ -k_{\mathrm{DMF}} & k_{\mathrm{DMF}} + \dfrac{k_{\mathrm{GB1}}}{\tau_1^2} & -\dfrac{k_{\mathrm{GB1}}}{\tau_1} & 0 & 0 \\ 0 & -\dfrac{k_{\mathrm{GB1}}}{\tau_1} & k_{\mathrm{GB1}} + k_{\mathrm{SA1}} & -k_{\mathrm{SA1}} & 0 \\ 0 & 0 & -k_{\mathrm{SA1}} & k_{\mathrm{SA1}} + k_{\mathrm{SA2}} & -\dfrac{k_{\mathrm{SA2}}}{\tau_2} \\ 0 & 0 & 0 & -\dfrac{k_{\mathrm{SA2}}}{\tau_2} & \dfrac{k_{\mathrm{SA2}}}{\tau_2^2} \end{bmatrix}. \tag{A.1}$$

As stated in Section 3.1 with regard to the electric motor control, it is worth observing that the proportional gain k_P appears in the damping matrix, while the integral gain k_I appears in the stiffness matrix.

Symbols and Abbreviations

B: Brake
CSD: Cross-Power Spectral Density
D: Brake disk
DCT: Dual Clutch Transmission
DFT: Discrete Fourier Transform
dof: Degree of freedom
Diff: DCT differential
DMF: Dual Mass Flywheel
E: Encoder
FRF: Frequency Response Function
HiL: Hardware-in-the-Loop
I: Mass moment of inertia
ICE: Internal Combustion Engine
M1/M2: Electric motors
MT: Manual Transmission
PSD: Power Spectral Density
SA1/SA2: Half shafts
k: Torsional stiffness
j: Imaginary unit
β: Viscous damping coefficient
$\theta, \dot{\theta}, \ddot{\theta}$: Angular position, speed, and acceleration
τ_1: Gear ratio ($\dot{\theta}_{\mathrm{in}}/\dot{\theta}_{\mathrm{out}}$) of the DCT
τ_2: Gear ratio of the MT
Ω: Angular frequency
T: Torque
T1/T2: Torque sensors
$[\alpha]$: Receptance matrix
$[B]$: Damping matrix
$[K]$: Stiffness matrix
$[M]$: Mass matrix
$\{\psi\}_i$: ith natural mode
ω_i: Natural frequency of ith mode.

Conflict of Interests

The authors declare that there is no conflict of interests regarding the publication of this paper.

References

[1] P. Bellomo, N. De Vito, C. Lang, and L. Scamardi, "In depth study of vehicle powertrains to identify causes of loose components rattle in transmissions," SAE Technical Paper 2002-01-0702, 2002.

[2] E. Galvagno, D. Morina, A. Sorniotti, and M. Velardocchia, "Drivability analysis of through-the-road-parallel hybrid vehicles," *Meccanica*, vol. 48, no. 2, pp. 351–366, 2013.

[3] S. Nastac and A. Leopa, "New structural configurations for vibroisolation devices with high isolation performances," *WSEAS Transactions on Applied and Theoretical Mechanics*, vol. 3, no. 5, pp. 155–164, 2008.

[4] L. Q. Song, L. P. Zeng, S. P. Zhang, J. D. Zhou, and H. E. Niu, "Design and analysis of a dual mass flywheel with continuously variable stiffness based on compensation principle," *Mechanism and Machine Theory*, vol. 79, pp. 124–140, 2014.

[5] E. Galvagno, M. Velardocchia, A. Vigliani, and A. Tota, "Experimental analysis and model validation of a dual mass flywheel for passenger cars," in *Proceedings of the SAE World Congress & Exhibition*, SAE Technical Paper no. 2015-01-1121, pp. 1–8, Detroit, Mich, USA, April 2015.

[6] Z. Zhang, R. Singh, and A. R. Crowther, "Limitations of smoothening functions for automotive vibro-impact problems," *Shock and Vibration*, vol. 18, no. 1-2, pp. 397–406, 2011.

[7] A. Farshidianfar, H. Moeenfard, and A. Rafsanjani, "Frequency response calculation of non-linear torsional vibration in gear systems," *Proceedings of the Institution of Mechanical Engineers, Part K: Journal of Multi-body Dynamics*, vol. 222, no. 1, pp. 49–60, 2008.

[8] A. Farshidianfar, M. Ebrahimi, and H. Bartlett, "Hybrid modelling and simulation of the torsional vibration of vehicle driveline systems," *Proceedings of the Institution of Mechanical Engineers, Part D: Journal of Automobile Engineering*, vol. 215, no. 2, pp. 217–229, 2001.

[9] M. T. Menday, H. Rahnejat, and M. Ebrahimi, "Clonk: an onomatopoeic response in torsional impact of automotive drivelines," *Proceedings of the Institution of Mechanical Engineers, Part D*, vol. 213, no. 4, pp. 349–357, 1999.

[10] E. Galvagno, A. Tota, M. Velardocchia, and A. Vigliani, "Test bench characterisation and frequency domain torsional model validation of transmission systems and components," in *Proceedings of the TrC-IFToMM Symposium on Theory of Machines and Mechanisms*, pp. 1–9, Izmir, Turkey, June 2015.

[11] Q. Chang, L. Hou, Z. Sun, Y. Wei, and Y. You, "Nonlinear modeling of helical gear pair with friction force and frictional torque," *WSEAS Transactions on Applied and Theoretical Mechanics*, vol. 9, no. 1, pp. 264–274, 2014.

[12] X. Jinli, S. Xingyi, and P. Bo, "Numerical analysis and demonstration: transmission shaft influence on meshing vibration in driving and driven gears," *Shock and Vibration*, vol. 2015, Article ID 365084, 10 pages, 2015.

[13] Y. Jin, J. Zhang, and X. Guan, "Theoretical calculation and experimental analysis of the rigid body modes of powertrain mounting system," *WSEAS Transactions on Applied and Theoretical Mechanics*, vol. 8, no. 3, pp. 193–201, 2013.

[14] E. Galvagno, G. R. Guercioni, and M. Velardocchia, "Experimental analysis and modeling of transmission torsional vibrations," in *Proceedings of the 6th International Conference on Automotive and Transportation Systems (ICAT '15)*, Salerno, Italy, June 2015.

[15] A. S. Mendes and P. S. Meirelles, "Application of the hardware-in-the-loop technique to an elastomeric torsional vibration damper," *SAE International Journal of Engines*, vol. 6, no. 4, pp. 2004–2014, 2013.

[16] A. Sorniotti, N. D'Alfio, E. Galvagno, A. Morgando, and F. Amisano, "Hardware-in-the-loop testing of automotive control systems," SAE Technical Paper 2006-01-1962, 2006.

[17] G. Bracco, E. Giorcelli, G. Mattiazzo, V. Orlando, and M. Raffero, "Hardware-In-the-Loop test rig for the ISWEC wave energy system," *Mechatronics*, vol. 25, pp. 11–17, 2015.

[18] E. Galvagno, M. Velardocchia, and A. Vigliani, "Dynamic and kinematic model of a dual clutch transmission," *Mechanism and Machine Theory*, vol. 46, no. 6, pp. 794–805, 2011.

[19] L. Meirovitch, *Fundamentals of Vibrations*, International Edition, McGraw-Hill, 2001.

[20] A. Brandt, *Noise and Vibration Analysis—Signal Analysis and Experimental Procedures*, John Wiley & Sons, Chichester, UK, 2010.

[21] P. D. Welch, "The use of fast Fourier transform for the estimation of power spectra: a method based on time averaging over short, modified periodograms," *IEEE Transactions on Audio and Electroacoustics*, vol. 15, no. 2, pp. 70–73, 1967.